Dissociative photoionization of NO across a shape resonance in the XUV range using circularly polarized synchrotron radiation

K. Veyrinas,[1,*] N. Saquet,[1,†] S. Marggi Poullain,[1,‡] M. Lebech,[2] J.-C. Houver,[1]
R. R. Lucchese,[3] and D. Dowek[1,§]
[1]Institut des Sciences Moléculaires d'Orsay (ISMO), CNRS, Univ. Paris-Sud, Université Paris-Saclay, F-91405 Orsay, France
[2]Niels Bohr Institute, University of Copenhagen, Copenhagen, Denmark
[3]Lawrence Berkeley National Laboratory, Berkeley, CA 94720, USA
(22 July 2019)

We report benchmark results for dissociative photoionization (DPI) spectroscopy and dynamics of the NO molecule in the region of the σ^* shape resonance in the ionization leading to the $NO^+(c\ ^3\Pi)$ ionic state. The experimental study combines well characterized XUV circularly polarized synchrotron radiation (SR), delivered at the DESIRS beamline (SOLEIL), with ion-electron coincidence 3D momentum spectroscopy. The measured (N^+, e) kinetic energy correlation diagrams reported at four discrete photon energies in the extended 23-33 eV energy range allow for resolving the different active DPI reactions, and indicate the importance of spectrally-resolved studies using SR in the context of time-resolved studies where PI is induced by broadband XUV attosecond pulses. In the dominant DPI reaction which leads to the $NO^+(c\ ^3\Pi)$ ionic state, PI dynamics across the σ^* shape resonance are probed by molecular frame photoelectron angular distributions where the parallel and perpendicular transitions are highlighted, as well as the circular dichroism $\mathrm{CDAD}(\theta_e)$ in the molecular frame. The latter also constitute benchmark references for molecular polarimetry. The measured dynamical parameters are well described by multichannel Schwinger configuration interaction calculations. Similar results are obtained for the DPI spectroscopy of highly excited NO^+ electronic states populated in the explored XUV photon energy range.

I. Introduction

Photoionization (PI) is a fundamental and ubiquitous process which constitutes a powerful tool for investigating structural properties and ultrafast dynamics in molecules. This light-matter interaction is best probed and understood at the level of the so-called molecular frame photoelectron angular distributions (MFPADs) [1]. Experimentally, these observables can be retrieved by measuring photoelectron angular distributions from aligned or oriented molecules or, as done in the present work, by means of ion-electron coincidence 3D momentum spectroscopy taking advantage of dissociative photoionization (DPI) processes/reactions in the axial recoil approximation.

MFPADs are sensitive to the symmetry of the initial (neutral) and final (ionic) molecular states, scattering of the photoelectron in the anisotropic potential of the molecular ion, electronic correlations induced by PI, and the symmetry and shape of the ionization continuum (*e.g.* resonances). Those complete observables give access to the amplitudes and relative phases of the complex dipole matrix elements [1]. As a result, numerous studies have been dedicated to the characterization of MFPADs for inner-valence shell [2–4] and inner shell [5–8] photoionization. In this paper, we report on the PI dynamics of the NO molecule

[*]Corresponding author: kevin.veyrinas@u-bordeaux.fr; Present address: Centre Lasers Intenses et Applications (CELIA), Domaine du Haut Carré, 43 rue Pierre Noailles, 33405 Talence Cedex, France.
[†]Present address: CAMECA, 29 Quai des Grésillons, 92622 Gennevilliers Cedex, France.
[‡]Present address: Departamento de Química, Módulo 13, Facultad de Ciencias, Universidad Autónoma de Madrid, 28049 Madrid, Spain.
[§]Corresponding author: danielle.dowek@u-psud.fr

across a shape resonance by studying the benchmarked DPI reaction given in Eq. (1), which will be referred to as process (I), in the 23-33 eV photon energy range:

$$\mathrm{NO}(X\,^2\Pi, 4\sigma^2 5\sigma^2 1\pi^4 2\pi^1) + h\nu \rightarrow \mathrm{NO}^+(c\,^3\Pi, (4\sigma)^{-1}) + \mathrm{e} \rightarrow \mathrm{N}^+(^3P) + \mathrm{O}(^3P) + \mathrm{e} \qquad (1)$$

This process involves the $c\,^3\Pi$ state of the NO^+ molecular ion, corresponding to ionization of the 4σ inner-valence shell molecular orbital, and dissociation into the $N^+(^3P) + O(^3P)$ first dissociation limit [9,10]. Using circularly polarized light (CPL), we probe the PI dynamics through MFPADs for all orientations of the molecular axis relative to the polarization axis of linearly polarized light, as well as the circular dichroism in the angular distribution (CDAD) which measures the variation of the MFPAD of an achiral molecule when exposed to left- or right-handed CPL [2,6,10–13].

As pointed out previously [10,14], the analytical expression of the MFPAD also encodes the complete polarization state of the ionizing radiation in terms of the normalized Stokes parameters (s_1, s_2, s_3), where (s_1, s_2) and (s_3) characterize the linearly and circularly polarized intensities, respectively, and $P = \sqrt{s_1^2 + s_2^2 + s_3^2}$ is the degree of polarization [15]. This remarkable property underlies the 'molecular polarimetry' (MP) method [16] which is tunable and available over a spectral range spanning from VUV to x-ray photon energies [14,17,18], where polarimetry is a challenging task. We recently applied the MP method to retrieve the complete polarization state of individual high-order harmonics (HHs) in an attosecond pulse train (APT) produced by the HHG-based XUV source of the PLFA facility of CEA-Saclay [19], for different schemes involving symmetry breaking in the generation process [20,21]. For these experiments, we chose process (I) which possesses fingerprint properties to act as an efficient 'polarimeter'. As MP requires the knowledge of the CDAD [16], the results reported in the present manuscript can be taken as references.

This paper is organized as follows. Section II briefly describes the methods in terms of the experimental setup for the vector correlation (VC) method based on ion-electron coincidence 3D momentum spectroscopy, the $F_{LN}(\theta_e)$ function formalism for experimentally extracting the MFPADs, and the theoretical details for computing the MFPADs. In Section III, we report the measured (E_{N+}, E_e) kinetic energy correlation diagrams (KECDs). We highlight the complementarity of this synchrotron study with experiments involving broadband XUV attosecond pulses. MFPADs and dynamical parameters characterizing the PI dynamics of process (I) across the shape resonance are then presented in Section IV. In Section V, we focus on the CDAD results and report reference terms for the MP method. We report in Section VI the main characteristics of new DPI channels involving highly excited states of NO^+ of Π and Σ symmetry, populated in the explored photon energy range. Finally, conclusions are given in Section VII.

II. Methods

A. Experimental setup

Experiments have been performed on the DESIRS VUV beamline at SOLEIL synchrotron facility [22], using the 8-bunch temporal structure mode (147-ns period, 50-ps pulse duration). Taking advantage of both the high spectral resolution and the variable polarization undulator coupled with an *in situ* VUV optical polarimeter [23], we studied the DPI reactions of the NO molecule induced by pure right-handed CPL (s_3 Stokes parameter higher than 0.99) at the following photon energies: 23.25, 26.35, 29.45 and 32.55 eV (with a spectral resolution

varying from 4 to 7.5 meV). The latter allow for sampling the σ^* shape resonance of the $NO^+(c\ ^3\Pi)$ ionic state, centered around $h\nu = 30$ eV, and correspond to the 15th, 17th, 19th and 21st harmonics of a 800-nm fundamental wavelength laser, respectively.

The vector correlation (VC) method [9] used here for performing coincidence ion-electron 3D momentum spectroscopy is based on the previously described double velocity spectrometer [24,25], which combines time of flight (TOF) measurement and impact position imaging technique. Briefly, the interaction region located at the center of the spectrometer is defined by the intersection between the supersonic molecular jet of NO and the synchrotron radiation (SR) beam. Ions and electrons are extracted from the interaction region and guided to their respective time and position sensitive detectors (TPSDs, DLD40, RoentDek) by a dc electric field $\boldsymbol{E}$ coupled to a set of focusing electrostatic lenses. The magnitude of the extraction field $\boldsymbol{E}$ has been varied from 30 V/cm (for $h\nu = 23.25$ eV) to 150 V/cm (for $h\nu = 32.55$ eV) such that a complete 4π collection of both ions and electrons of the DPI processes of interest is ensured. From the magnitude of the $\mathbf{V}_{N+}$ and $\mathbf{V}_e$ emission velocity vectors of the ion fragment and the photoelectron produced in a single DPI event, and the spatial analysis of the ($\mathbf{V}_{N+}$, $\mathbf{V}_e$, $\mathbf{k}$) vector correlation, where $\mathbf{k}$ is the light propagation axis, we extract the (E_{N+}, E_e) KECDs and the $I(\theta_e,\phi_e,\chi)$ MFPADs presented in sections III and IV, respectively.

B. Molecular frame photoemission via the F_{LN} formalism

In the dipole approximation, the expression of the MFPAD for one-photon PI of a linear molecule induced by circularly polarized light takes the remarkably simple form [10,11]:

$$\begin{aligned} I_{h=\pm1}(\theta_e,\phi_e,\chi) = F_{00}(\theta_e) - \frac{1}{2}F_{20}(\theta_e)P_2^0(\cos\chi) - \frac{1}{2}F_{22}(\theta_e)P_2^2(\cos\chi)\cos(2\phi_e) \\ - \frac{1}{2}F_{21}(\theta_e)P_2^1(\cos\chi)\cos(\phi_e) \pm F_{11}(\theta_e)P_1^1(\cos\chi)\sin(\phi_e) \end{aligned} \quad (2)$$

where χ is the polar angle defining the orientation of the molecular axis with respect to the light propagation axis $\mathbf{k}$, and (θ_e,ϕ_e) characterizes the photoelectron emission in the molecular frame. Left- (right-) handed circularly polarized light is defined by a positive (negative) helicity $h = +1$ ($h = -1$), and P_L^N are the associated Legendre polynomials.

The five one-dimensional $F_{LN}(\theta_e)$ functions contain all the dynamical information about the PI process and are partial-wave expanded in Legendre polynomials as:

$$F_{LN}(\theta_e) = \sum_{L'}^{L'_{max}} C_{L'LN} P_{L'}^N(\cos\theta_e) \quad (3)$$

where the $C_{L'LN}$ are expressed in terms of the dipole matrix elements [10,26] and L'_{max} is governed by the maximum orbital angular momentum carried away by the photoelectron. Briefly, simple linear combinations of $F_{00}(\theta_e)$ and $F_{20}(\theta_e)$ describe the polar dependence of the parallel $(\Delta\Lambda = 0)$ and perpendicular $(\Delta\Lambda = \pm 1)$ PI transitions after integration over ϕ_e. $F_{22}(\theta_e)$ characterizes in particular the azimuthal dependence of the perpendicular transition and provides insights into the symmetry of the initial and final molecular states involved. The

amplitude and sign of the relative phase between the dipole matrix elements for the parallel and perpendicular transitions are extracted from $F_{21}(\theta_e)$ and $F_{11}(\theta_e)$. The latter function, $F_{11}(\theta_e)$, characterizes the circular dichroism observed in the molecular frame. The measured $I(\theta_e,\phi_e,\chi)$ angular distribution allows for extracting the five $F_{LN}(\theta_e)$ functions according to Eq. (2).

C. Theoretical methods

The photoionization calculations were performed using multichannel Schwinger configuration interaction (MCSCI) method [27,28]. The current calculations are very similar to earlier calculations on the photoionization of NO [10,12,26,28]. Here we used a single-center expansion with $l_{max} = 60$, which is somewhat better converged than the previous calculations. The bound states were computed using an augmented correlation consistent polarized valence triple zeta (aug-cc-pVTZ) basis set [29,30] and a valance complete active space self-consistent field (CASSCF) calculation on the ground state of the molecule, which included 11 electrons in 8 active orbitals, four σ orbitals and four π orbitals, using MOLPRO [31]. The ground state CASSCF orbitals were used for both the neutral initial state and for the ion states. All calculations were computed with a fixed inter-nuclear distance of 1.15077 Å [32]. The *N*-electron initial state and (*N*-1)-electron final states were then computed using complete active space configuration interaction (CAS-CI) wave functions using the orbitals from the ground state CASSCF calculation. In all calculations the two 1s orbitals were always doubly occupied. In Table I we give the vertical ionization potentials computed in this manner and compare them to available experimental energies [33]. To compute the cross section for a given final ion state, we included in the coupled channels only states that are open at the energy of interest. Additionally, we included only those open states in the coupled channel calculation that had at least a 0.15 Mbarn cross section for an energy below 35 eV. For the cross sections for photoionization leading to the $c\ ^3\Pi$ we used the ten channels listed in the "a" calculation in Table I. Additionally for photoionization leading to this state, we adjusted the channel energies in the calculation to agree with the experimental values [33] listed in the table. For calculations for the photoionization leading to higher energy ion states, we just used the channel energies from the unadjusted MCSCI calculations, that are also given in Table I. For the $B'\ ^1\Sigma^+$ and $B\ ^1\Pi$ states at 23.35 eV we used the 11 channel "b" calculation. For the (4) $^3\Pi$ state at 29.45 eV we used the 15 channel "c" calculation.

State	E_{MCSCI} (eV)	Calc.	E_{exp} (eV)	Configurations
$X\ ^2\Pi$	0		0	$(4\sigma)^2(5\sigma)^2(1\pi)^4(2\pi)^1$
$X\ ^1\Sigma^+$	9.39	a, b, c	9.72	$(4\sigma)^2(5\sigma)^2(1\pi)^4(2\pi)^0$
$a\ ^3\Sigma^+$	16.21	a, b, c	16.28	$(4\sigma)^2(5\sigma)^2(1\pi)^3(2\pi)^1$
$b\ ^3\Pi$	16.78	a, b, c	16.61	$(4\sigma)^2(5\sigma)^1(1\pi)^4(2\pi)^1$
$w\ ^3\Delta$	17.56	a, b, c	17.37	$(4\sigma)^2(5\sigma)^2(1\pi)^3(2\pi)^1$
$b'\ ^3\Sigma^-$	18.16	a, b, c	18.18	$(4\sigma)^2(5\sigma)^2(1\pi)^3(2\pi)^1$
$A'\ ^1\Sigma^-$	18.69	a, b, c	18.50	$(4\sigma)^2(5\sigma)^2(1\pi)^3(2\pi)^1$
$A\ ^1\Pi$	18.78	a, b, c	18.48	$(4\sigma)^2(5\sigma)^1(1\pi)^4(2\pi)^1$
$W\ ^1\Delta$	18.93	a, b, c	18.69	$(4\sigma)^2(5\sigma)^2(1\pi)^3(2\pi)^1$
$c\ ^3\Pi$	22.00	a, b, c	21.70	$(4\sigma)^1(5\sigma)^2(1\pi)^4(2\pi)^1$
$B\ ^1\Pi$	23.82	a, b, c	23.15	$(4\sigma)^1(5\sigma)^2(1\pi)^4(2\pi)^1+(4\sigma)^2(5\sigma)^1(1\pi)^3(2\pi)^2$
$B'\ ^1\Sigma^+$	24.68	b, c		$(4\sigma)^2(5\sigma)^2(1\pi)^3(2\pi)^1 + (4\sigma)^2(5\sigma)^2(1\pi)^2(2\pi)^2$
(2) $^3\Sigma^-$	26.42	c		$(4\sigma)^2(5\sigma)^0(1\pi)^4(2\pi)^2$

(4) $^3\Pi$	26.50	c	$(4\sigma)^2(5\sigma)^1(1\pi)^3(2\pi)^2$
(2) $^1\Sigma^+$	26.79	c	$(4\sigma)^2(5\sigma)^2(1\pi)^2(2\pi)^2 + (4\sigma)^2(5\sigma)^2(1\pi)^3(2\pi)^1$
(3) $^1\Pi$	27.72	c	$(4\sigma)^2(5\sigma)^1(1\pi)^3(2\pi)^2 + (4\sigma)^1(5\sigma)^2(1\pi)^4(2\pi)^1$

TABLE I. States included in the different coupled channel calculations with computed MCSCI vertical energies, experimental vertical energies [33], and primary electronic configurations in the ionic states. All configurations start with $(1\sigma)^2(2\sigma)^2(3\sigma)^2$ with the most important configuration given first. Calculation "a" contained 10 states, calculation "b" contained 11 states, and calculation "c" contained 15 states.

III. (E_{N+}, E_e) kinetic energy correlation diagrams

A. Photoionization by synchrotron radiation at $h\nu$ = 23.25, 26.35, 29.45 and 32.55 eV

In this work, we only consider the (N^+, e) coincident events since DPI leads to a preponderant production of N^+ ions compared to O^+ for the studied energy region [34]. Fig. 1(a-d) displays the (E_{N+}, E_e) KECDs for PI induced by SR at the four photon energies $h\nu$ = 23.25, 26.35, 29.45 and 32.55 eV, in which the (N^+, e) events are plotted as a function of the E_{N+} ion fragment and E_e photoelectron kinetic energies. In these two-dimensional histograms, each structure defined by the (E_{N+}, E_e) coordinates corresponds to a particular DPI process and, as a consequence of energy and momentum conservation, all DPI processes lie along straight lines, each one corresponding to a different open dissociation limit (see Table II). Given the 4π collection of both ions and electrons achieved here, integrating the number of events of each peak provides the branching ratios (BRs) among the different DPI processes.

At the four energies displayed in Fig. 1(a-d), the brightest peak (BR varying from 80 % at 23.25 eV to 45 % at 32.55 eV) is observed for a constant N^+ fragment energy (E_{N+} ~ 0.4 eV) while the photoelectron carries the excess energy above the ionization threshold of the $c\ ^3\Pi$ ionic state of NO^+ (E_e ~ 1.5, 4.6, 7.7 and 10.8 eV), reflecting that photoionization takes place before dissociation to the L_1 dissociation limit. It corresponds to process (I) assigned to direct ionization into the $NO^+(c\ ^3\Pi, v = 0)$ bound state followed by dissociation to the limit L_1 (Eq. (1)). This DPI process has been most completely characterized for a photon energy of $h\nu$ = 23.64 eV [9,10,26]. Using higher extraction fields $\boldsymbol{E}$ to maintain the 4π collection of photoelectrons results in a broadening of the peak in the KECD along the E_e axis, from 270 meV (Fig. 1(a), E = 30 V/cm) to 1.7 eV (Fig. 1(d), E = 150 V/cm) at full width at half maximum (FWHM).

As the photon energy increases, more and more ionization continua of NO^+ excited states are energetically available as well as more dissociation limits becoming open, resulting in a growing number of (N^+, e) DPI processes as observed in Fig. 1(a-d) and discussed in Section VI. Although six $N^+ + O$ dissociation channels are involved at these photon energies [35], some lie at nearby energies (see Table II) so that only three limits corresponding to L_1, $L_{2/3}$ and $L_{4/5/6}$ are distinguished in the KECDs. The elongated shape of these additional structures labeled II to V along the L_1, $L_{2/3}$ and $L_{4/5/6}$ dissociation limits indicates the repulsive character of the corresponding NO^+ excited states in the $NO(X\ ^2\Pi)$ Franck-Condon (FC) region. Despite the increasing complexity of the KECDs, most processes, which would not be identified in photoelectron or photoion spectra, can be resolved.

Finally, prior to analyzing process (I) and getting for each photon energy the MFPADs reported in the next section, one performs a double E_{N+} and E_e selection of the (N^+, e) coincident events, as shown by the gray dashed rectangle in Fig. 1(a).

Label	Dissociation products	Energy (eV)
L_1	$N^+(^3P) + O(^3P)$	21.031

L_2	$N^+ (^1D) + O(^3P)$	22.930
L_3	$N^+ (^3P) + O(^1D)$	22.998
L_4	$N^+ (^1D) + O(^1D)$	24.897
L_5	$N^+ (^1S) + O(^3P)$	25.083
L_6	$N^+ (^3P) + O(^1S)$	25.220

TABLE II. Dissociation limits of NO^+ leading to N^+ + O fragments [35].

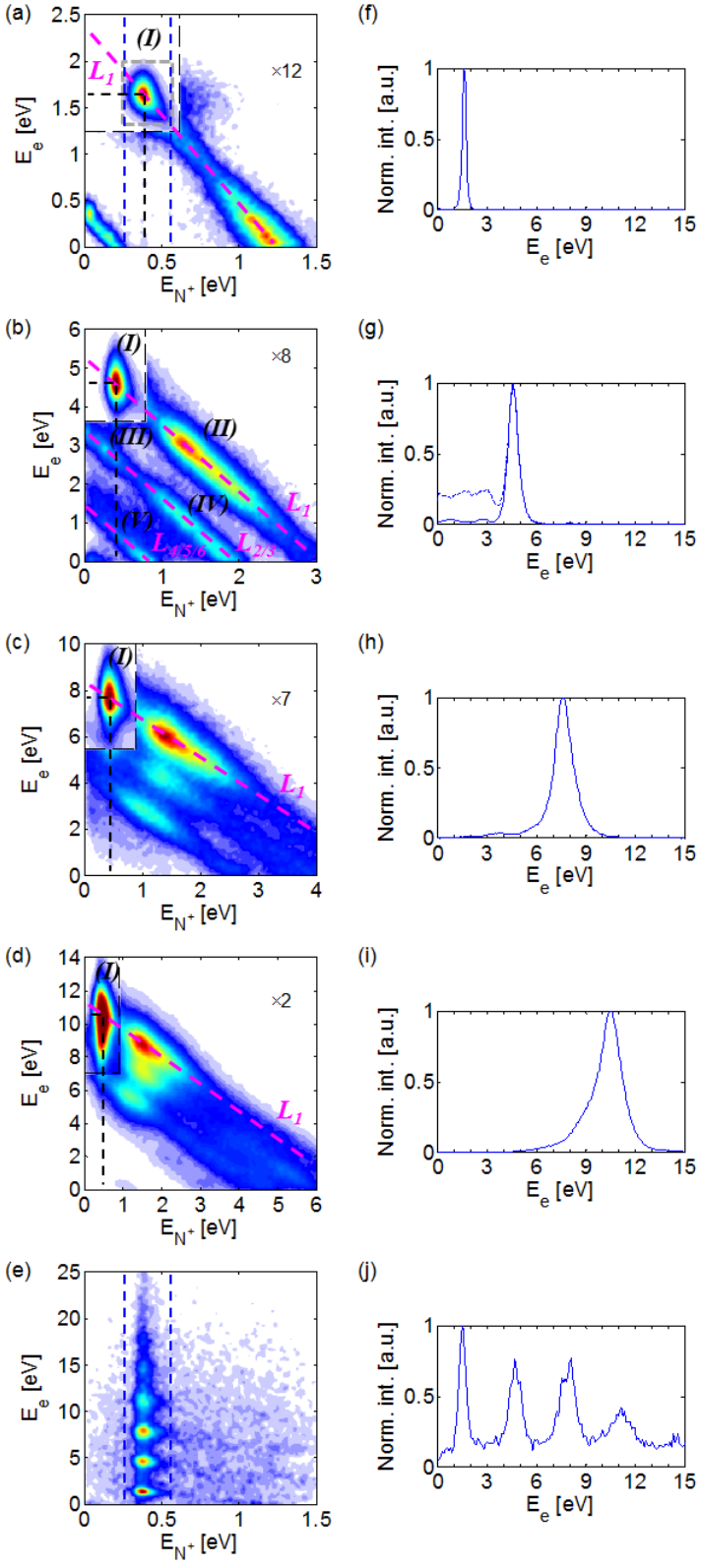

FIG. 1. (Color online) (E_{N+}, E_e) KECDs characterizing the DPI of NO induced by synchrotron radiation at (a) $h\nu$ = 23.25 eV, (b) $h\nu$ = 26.35 eV, (c) $h\nu$ = 29.45 eV, (d) $h\nu$ = 32.55 eV, photon energies corresponding to the 15th, 17th, 19th and 21st harmonics of a 800-nm fundamental wavelength laser, respectively, and (e) by an APT generated in randomly oriented SF_6 molecules [20]. The intensity scale runs from white (minimum) to red (maximum), with 12 ×, 8 ×, 7 × and 2 × amplification factors of the bottom and right parts of the KECDs relative to the top left corner. The pink dashed lines represent the dissociation limits while the E_{N+} and E_e kinetic energies associated to process (I) are identified by black dashed lines. (f-j) Corresponding photoelectron kinetic energy spectra: (full line) applying the 0.25 eV ≤ E_{N+} ≤ 0.55 eV selection on the ion fragment kinetic energy as depicted in (a) and (e) by the blue dashed lines, and (dashed line in (g)) without any selection. The gray dashed square in (a) indicates the double E_{N+} and E_e selection of the (N^+, e) coincident events.

B. Relevance for photoionization by attosecond pulses

This study illustrates the input of frequency-resolved synchrotron-based measurements to support the analysis of time-resolved studies, in which a broadband XUV attosecond pulse produced by high-order harmonic generation (HHG) is used as a pump or probe pulse. The major difference when studying DPI induced by such ultrashort pulses, compared to using SR, comes from their inherent spectral structure: a given PI process is induced by several harmonics, and the higher the harmonic energy, the larger the number of induced DPI processes. In that case, disentangling the various DPI reactions becomes intricate as overlaps between processes are likely to occur.

Regarding DPI of the NO molecule, all harmonics with energies higher than the ionization potential of the $c\ ^3\Pi$ state of NO^+ (IP = 21.73 eV), which is the lowest ionic state above the first dissociation limit (see Table I), contribute to the $N^+ + O$ DPI signal. As an example, Fig. 1(e) presents the KECD resulting from DPI of NO induced by an attosecond pulse train (APT) generated in randomly oriented SF_6 molecules by elliptically polarized infrared pulses (λ = 800 nm) [20]. It is noted that in that case the extraction field was chosen to ensure a 4π collection of low-energy ions ($E_{N+} \leq 0.55$ eV) and a strong discrimination against more energetic N^+ ions. The convolution of the typical HHG spectra produced in this experiment with the $NO^+(c\ ^3\Pi)$ total cross section in the corresponding energy range [34,36] led to the main contribution from harmonics H15 to H21 to process (I). Thus, Fig. 1(e) is expected to match the superposition of the four KECDs displayed in Fig. 1(a-d), for $E_{N+} \leq 0.55$ eV, weighted by the relative intensities of the different harmonics in the HHG spectrum.

As emphasized above, process (I) is characterized by the central energy $E_{N+} \sim 0.4$ eV and a 0.25 eV ≤ E_{N+} ≤ 0.55 eV well defined ion fragment kinetic energy range, represented by the blue dashed lines in Fig. 1(a) and (e). Applying first this selection to the KECDs Fig. 1(a-e) leads to the filtered photoelectron energy spectra displayed in Fig. 1(f-j). Beyond the dominant character of reaction (I) for each wavelength in Fig. 1(a-d), further amplified when the E_{N+} selection is performed in Fig. 1(f-i), we observe that the E_e energy bands assigned to process (I) do not encounter any overlap with other DPI processes induced by the other considered photon energies (which would not be the case without this selection, see the dashed line in Fig. 1(g)).

These results therefore ensure that the brightest peaks resolved in Fig. 1(e), lying vertically along the same $E_{N+} \sim 0.4$ eV ion fragment kinetic energy and separated by 3.1 eV, can be certainly assigned to process (I) induced by harmonics H15-H21 (contributions from H23 and H25 are also visible at higher photoelectron kinetic energies), without overlapping other DPI processes.

IV. Photoionization dynamics across the $4\sigma \rightarrow \sigma^*$ shape resonance

A. $F_{LN}(\theta_e)$ functions for PI to the $NO^+(c\ ^3\Pi)$ ionic state

Fig. 2 presents the complete set of retrieved $F_{LN}(\theta_e)$ functions, as well as the CDAD(θ_e) parameter (see Section IV. C.), describing process (I) induced by right-handed CPL at the four considered photon energies, compared with 10-state MCSCI calculations of the MFPADs in the velocity gauge. They display clear oscillations corresponding to sharply structured MFPADs and a remarkable CDAD parameter which amounts to large positive values. The fairly good agreement between experiment and theory over a 10-eV photon energy range is remarkable. MCSCI calculations involving a higher number of NO^+ states (up to 15 states, see Section II. C.), performed in the velocity and length gauges, only weakly influence the results for the description of process I. For this process, however, a better agreement with experiment is obtained using the velocity gauge. A convolution of the calculations with the apparatus function shows that the instrumental widths have only a minor influence on the extraction of the $F_{LN}(\theta_e)$ functions. Based on this fair agreement between the measured and computed $F_{LN}(\theta_e)$ functions at the studied photon energies, we refer to the calculations reported in ref. [10] in the 25-40 eV range for the main features of the complex dipole matrix elements and their evolution across the shape resonance. A specific discussion of the extraction of the dipole matrix elements in an extended photon energy range will be presented in a forthcoming paper.

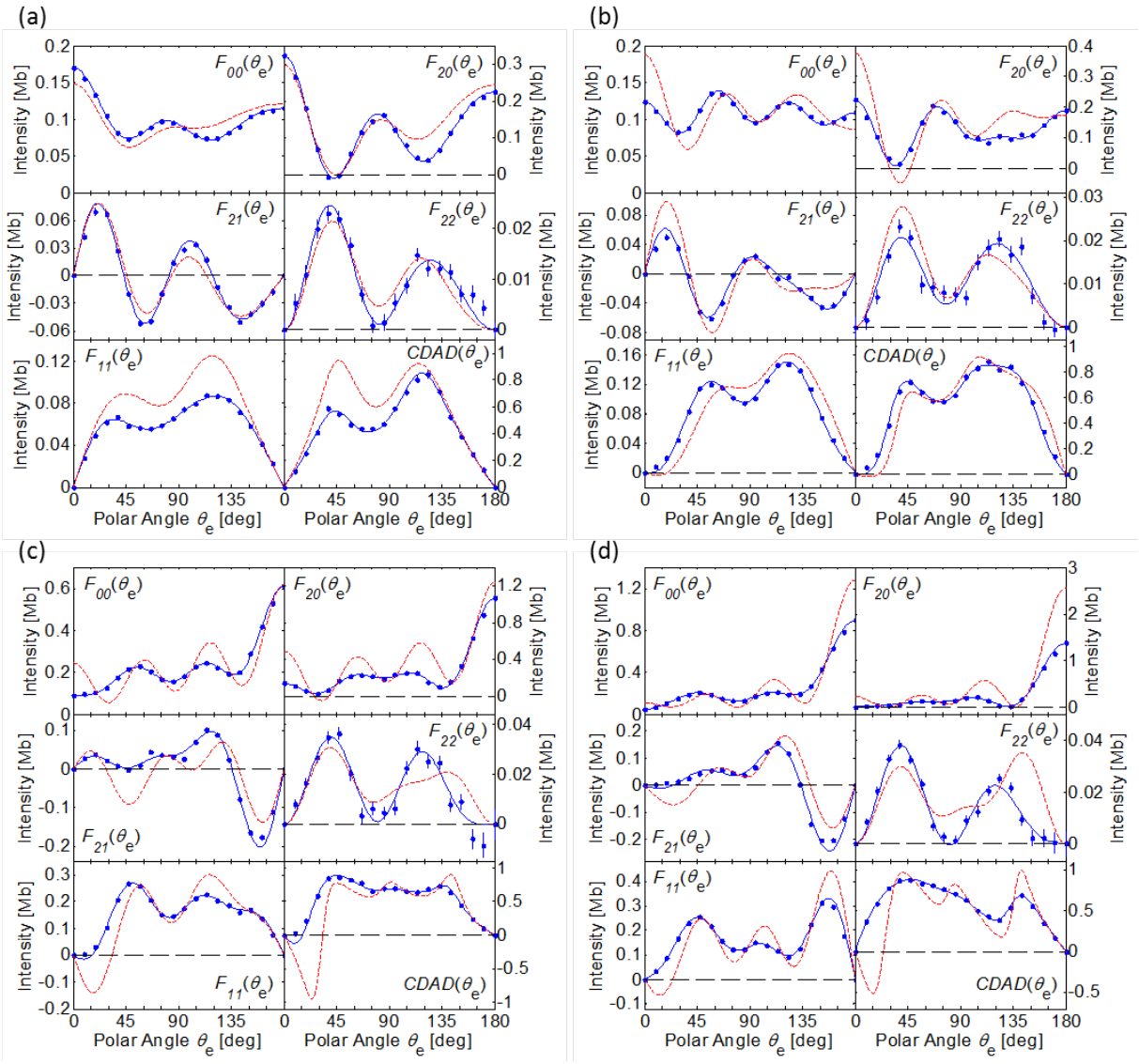

FIG. 2. (Color online) $F_{00}(\theta_e), F_{20}(\theta_e), F_{21}(\theta_e), F_{22}(\theta_e), F_{11}(\theta_e)$ functions and $CDAD(\theta_e)$ parameter describing process (I) induced by right-handed CPL at (a) $h\nu$ = 23.25 eV, (b) $h\nu$ = 26.35 eV, (c) $h\nu$ = 29.45 eV, and (d) $h\nu$ = 32.55 eV. Blue dots, experimental results with statistical error bars; blue line, Legendre polynomial fit (according to Eq. (3)); red dashed line, theoretical results. Experiment is normalized on theory such that the total cross section $\int_0^{\pi} F_{00}(\theta_e)\sin(\theta_e)d\theta_e$ is identical.

Here we emphasize the power of the F_{LN} expansion. From a single experiment using CPL, the knowledge of the five $F_{LN}(\theta_e)$ functions enables us to directly reconstruct, according to Eq. (2), the 3D MFPAD $I_\chi(\theta_e,\phi_e)$ for any orientation χ of the molecule relative to the propagation axis of light [14]. Besides, such an experiment is 'complete' as it also allows for retrieving, for the same DPI process, the MFPADs induced by linearly polarized light for any orientation χ of the molecule relative to the polarization axis, described by the subset of the four $F_{00}(\theta_e)$, $F_{20}(\theta_e)$, $F_{21}(\theta_e)$ and $F_{22}(\theta_e)$ functions [14].

B. MFPADs for parallel and perpendicular transitions

When studying PI dynamics of linear molecules induced by linearly polarized light, two geometries are of particular interest, featuring namely the parallel and perpendicular PI transitions. They correspond to an orientation of the molecular axis either parallel ($\chi = 0°$) or perpendicular ($\chi = 90°$) to the polarization axis of the ionizing radiation, respectively. For any other orientation χ of the molecular axis, or when considering circularly polarized light, the PI process is described as a coherent superposition of the PI amplitudes of these two transitions leading to complex MFPADs. For one-photon PI in the dipole approximation, the transition is characterized by the β_{ion} asymmetry parameter describing the recoil ion angular distribution in the axial recoil approximation, ranging from -1 (purely perpendicular) to 2 (purely parallel). In the 23-33 eV photon energy range studied in this work, process (I) is characterized by a large positive asymmetry parameter ($\beta_{N+} \sim 1$), reflecting the dominant parallel character of the electric dipole transition.

Fig. 3 displays the measured and computed MFPADs characterizing the parallel transition of process (I) for the four considered photon energies. The MFPAD, which preserves the cylindrical symmetry inherent to this geometry, shows a remarkable evolution across the shape resonance ($4\sigma \rightarrow \sigma^*$). As the photon energy increases, the dominant contribution in the continuum evolves from a $d\sigma$ to an $f\sigma$ partial wave. A strong anisotropy in the photoelectron emission enhanced towards the oxygen side of the NO molecule develops, consistent with the remarkable increase in the computed phases of the $s\sigma$ and $f\sigma$ dipole matrix elements across the resonance relative to the non-resonant $d\sigma$ matrix elements [10].

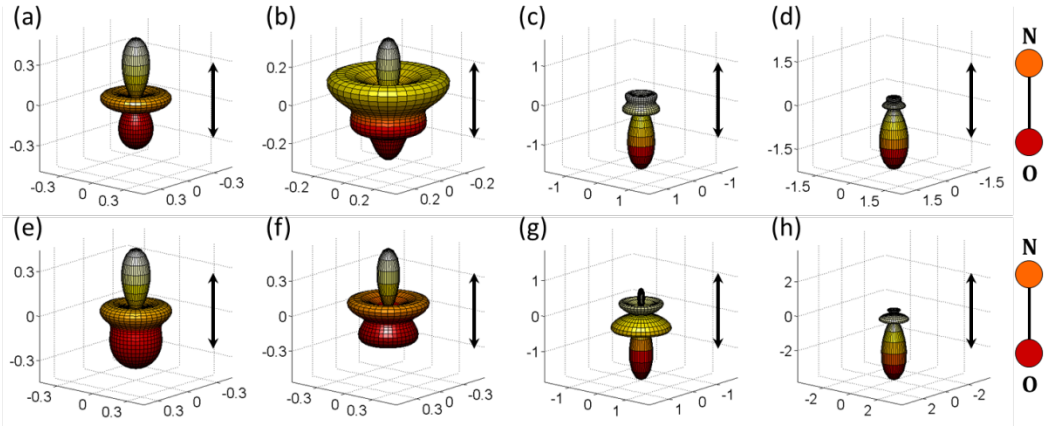

FIG. 3. (Color online) Measured (a-d) and computed (e-h) $I_{\chi=0°}(\theta_e)$ MFPADs characterizing the parallel transition of process (I) for $h\nu$ = 23.25, 26.35, 29.45 and 32.55 eV (from left to right).

As for the perpendicular PI transition, the shape of the MFPADs in Fig. 4 is dominated by a $d\pi$ partial wave in the continuum and displays only a weak energy dependence in the considered photon energy range. The noteworthy azimuthal dependence exhibited by the MFPADs reflects the loss of the cylindrical symmetry when the molecular axis is not oriented along the polarization axis ($\chi \neq 0°$). The favored emission in the plane defined by the molecular and polarization axes described by $F_{22}(\theta_e) > 0$ is a fingerprint of the one-electron character of the $NO^+(c\ ^3\Pi, (4\sigma)^{-1})$ ionization process, where the 2π outer electron is a spectator. The $NO(X\ ^2\Pi) \rightarrow NO^+(c\ ^3\Pi, (4\sigma)^{-1})$ reaction behaves like a $\Sigma^+ \rightarrow \Sigma^+$ transition and satisfies the corresponding relation between the $F_{LN}(\theta_e)$ functions [37]:

$$F_{00}(\theta_e) - \frac{1}{2} F_{20}(\theta_e) = 3F_{22}(\theta_e) \tag{4}$$

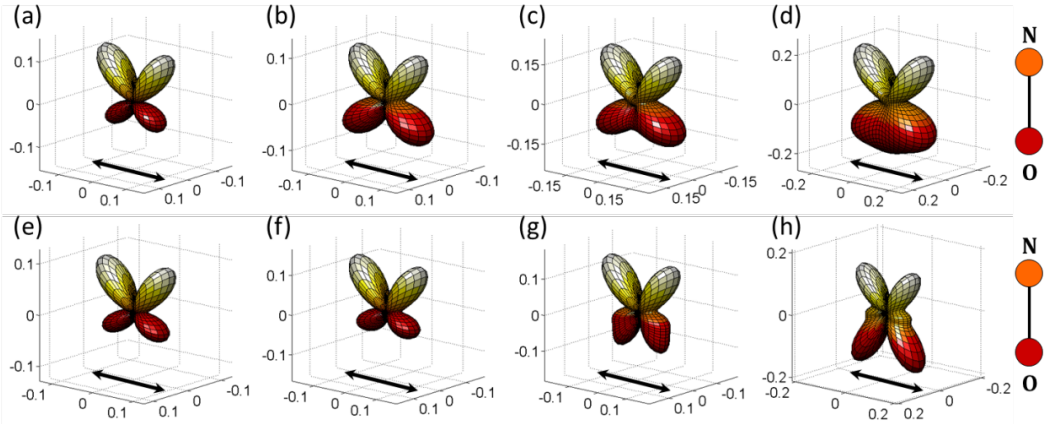

FIG. 4. (Color online) Measured (a-d) and computed (e-h) $I_{\chi=90°}(\theta_e,\phi_e)$ MFPADs characterizing the perpendicular transition of process (I) for $h\nu$ = 23.25, 26.35, 29.45 and 32.55 eV (from left to right).

These results, consistent with the overall behavior previously observed [38], highlight the completeness of the method.

C. Circular dichroism in the angular distribution

The circular dichroism in the angular distribution (CDAD) measures the variation of the MF photoemission of achiral molecules when exposed to left- or right-handed CPL [2,6,10,12,13]. It originates from the spatial chirality of the 'light-molecule' combined system induced by the non-coplanarity of three vectors: the $\mathbf{V}_{N+}$ ion fragment emission momentum, which gives the molecular axis in the axial recoil approximation, the $\mathbf{V}_e$ photoelectron emission momentum, and the light propagation axis **k** [12]. The CDAD results from the asymmetry in the MFPAD which reverses when the sign of the helicity h of the ionizing light is changed. The CDAD is largest when the molecular axis is oriented perpendicular to the light propagation axis.

Fig. 5 displays the measured MFPADs (a-d), reconstructed from the $F_{LN}(\theta_e)$ functions presented in Fig. 2 according to Eq. (2), and the computed ones (i-l), associated with process (I) for this geometry, $I_{\chi=90°}(\theta_e,\phi_e)$, induced by right-handed CPL at $h\nu = 23.25$, 26.35, 29.45 and 32.55 eV. These MFPADs exhibit a large left-right asymmetry: the photoelectron is preferentially emitted on the left half sphere, as highlighted by the cuts of the 3D MFPADs in the polarization plane ($\phi_e = 90°$ and $\phi_e = 270°$) represented in Fig. 5(e-h), characteristic of a strong circular dichroism. The "sign" of this asymmetry, and so the circular dichroism, remains the same in the explored photon energy range and constitutes a robust character along the shape resonance in the ionization continuum of the $c\,^3\Pi$ state of NO^+ [3,10].

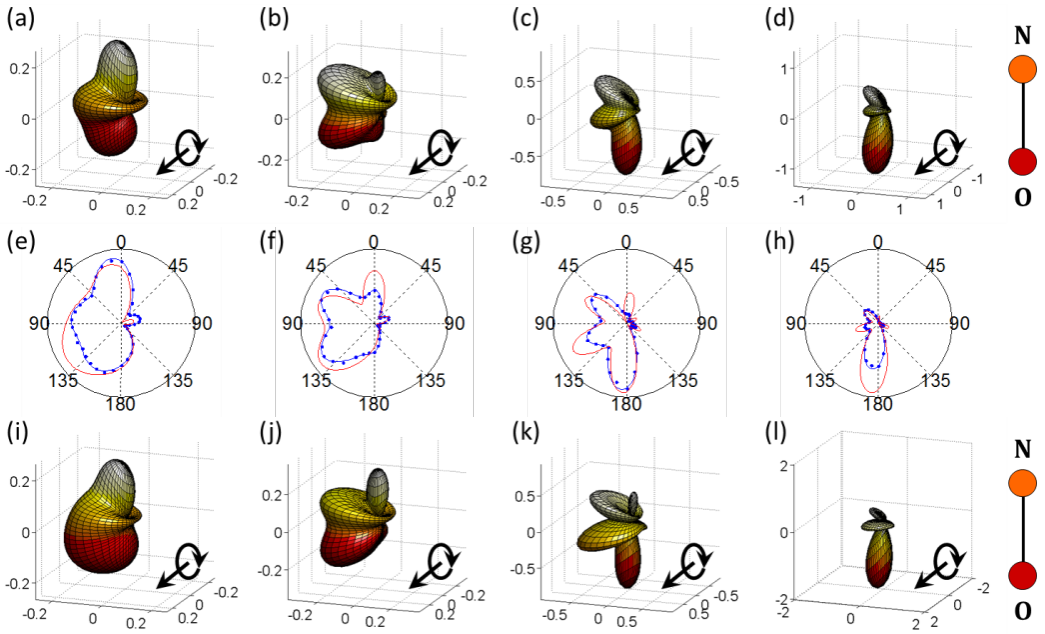

FIG. 5. (Color online) Measured (a-d) and computed (i-l) $I_{\chi=90^\circ}(\theta_e,\phi_e)$ MFPADs for an orientation of the molecular axis perpendicular to the light propagation axis, describing process (I) induced by right-handed CPL at $h\nu$ = 23.25, 26.35, 29.45 and 32.55 eV (from left to right). (e-h) Corresponding cuts of the measured (blue) and computed (red) 3D MFPADs in the polarization plane (right half $\phi_e = 90°$ and left half $\phi_e = 270°$).

The MF circular dichroism is characterized by the $F_{11}(\theta_e)$ function or, for convenience, in terms of the dimensionless $\mathrm{CDAD}(\theta_e)$ parameter. When the molecule is oriented perpendicular to the propagation axis of light ($\chi = 90°$), as in Fig. 5, $\mathrm{CDAD}(\theta_e)$ is defined as the relative variation of the MF photoemission in the polarization half plane ($\phi_e = 90°$) when the helicity h of the light is changed from +1 (left-handed CPL) to -1 (right-handed CPL). For a given helicity ($h = +1$), it is also obtained from the left-right emission asymmetry in the polarization plane ($\phi_e = 90°$ or $270°$) [12]:

$$\mathrm{CDAD}(\theta_e) = \frac{I_{+1,90} - I_{-1,90}}{I_{+1,90} + I_{-1,90}} = \frac{I_{+1,90} - I_{+1,270}}{I_{+1,90} + I_{+1,270}} = \frac{2F_{11}(\theta_e)}{2F_{00}(\theta_e) + \frac{1}{2}F_{20}(\theta_e) + 3F_{22}(\theta_e)} \quad (5)$$

Fig. 2 presents the measured and computed $F_{11}(\theta_e)$ and $\mathrm{CDAD}(\theta_e)$ parameters corresponding to the MFPADs displayed in Fig. 5, respectively. Because it involves $F_{00}(\theta_e), F_{20}(\theta_e)$ and $F_{22}(\theta_e)$ in the denominator, $\mathrm{CDAD}(\theta_e)$ is more sensitive to any default in extracting each of them. In this photon energy range, $F_{11}(\theta_e)$ and $\mathrm{CDAD}(\theta_e)$ do not change sign, reach significantly high values ($\mathrm{CDAD}(\theta_e)$ close to 1) and are positive, the latter feature reflecting the photoemission favored in the left polarization half plane ($\phi_e = 270°$) for right-handed CPL as depicted in Fig. 5.

V. Reference $F_{11}(\theta_e)$ functions for molecular polarimetry

As mentioned in the Introduction, based on the remarkable sensitivity of the MFPADs to the polarization state of the ionizing radiation, we demonstrated a 'molecular polarimetry' (MP) method allowing for the determination of the amplitude and sign of all three (s_1, s_2, s_3) Stokes parameters [16] describing the hitherto unknown complete polarization state. The expression of the MFPAD induced by such radiation, $I(\theta_e, \phi_e, \chi, \gamma)$, now requires the introduction of an additional azimuthal angle γ to define the orientation of the molecular axis with respect to the light propagation axis [10,14]. As discussed above for CPL, the measured $I(\theta_e, \phi_e, \chi, \gamma)$ angular distribution provides the four $F_{00}(\theta_e)$, $F_{20}(\theta_e)$, $F_{21}(\theta_e)$, $F_{22}(\theta_e)$ functions, however it now gives access to the product $-s_3 \times F_{11}(\theta_e)$. Similarly, the quantity $\frac{I_{+1,90} - I_{+1,270}}{I_{+1,90} + I_{+1,270}}$ is equal to $-s_3 \times \mathrm{CDAD}(\theta_e)$. Retrieving the amplitude and sign of the s_3 Stokes parameter thus relies on the knowledge of measured or computed $F_{11}(\theta_e)$ and $\mathrm{CDAD}(\theta_e)$ parameters [16]: they are displayed here for the four considered photon energies. Despite the fair agreement between experiment and theory, measured reference values provide the most precise determination of s_3. Nevertheless, these calculations, in particular in the velocity gauge, still constitute a solid reference when experimental data are not available. For a further description and a quantitative use of $F_{11}(\theta_e)$, we present in Table III the measured (top) and computed (bottom) $C_{L'11}$ coefficients for the four considered photon energies. They are derived from the partial-wave expansion of the $F_{11}(\theta_e)$ function in Legendre polynomials up to the eighth order: the significant coefficients are presented here up to $L'_{\max} = 6$, according to Eq. (3).

hν (eV)	C_{111}	C_{211}	C_{311}	C_{411}	C_{511}	C_{611}
23.25	0.91	-0.08	0.11	0.05	0.01	0.01
26.35	1.19	-0.10	0.10	0.00	-0.09	-0.01
29.45	1.08	0.01	0.14	-0.01	-0.06	-0.08
32.55	0.88	0.04	0.26	-0.09	0.08	-0.11
23.25	1.242	-0.104	0.131	0.076	-0.020	-0.003
26.35	1.249	-0.237	0.046	-0.049	-0.055	-0.000
29.45	1.102	-0.185	0.053	-0.060	-0.165	-0.094
32.55	0.864	-0.061	0.198	-0.126	0.089	-0.226

TABLE III. Measured (top) and computed (bottom) $C_{L'11}$ coefficients for the four considered photon energies. Statistical error bars are of the order of 0.01. Experiment and theory are normalized such that the first coefficient C_{000} of $F_{00}(\theta_e)$ is equal to 1.

VI. Dissociative photoionization into highly excited states of NO^+

As pointed out in Section III, although process (I) is the dominant DPI channel in the explored photon energy range, additional ionic states mainly repulsive in the FC region are populated with increasing excitation energy. The main characteristics of some selected DPI channels, named as processes II to VII, are reported here for completeness in terms of

branching ratio, asymmetry parameters and MFPADs, and compared with the prediction of MCSCI calculations. Processes II to V have been labeled in the KECD reported in Fig. 1(b). In order to improve the resolution of such processes, three complementary experiments based on lower extraction fields than those used for the study of process (I) were performed at $h\nu = 26.35$, 29.45 and 32.55 eV (H17-H19-H21) photon energies, aiming at a 4π collection of electrons and ions in a restricted (E_{N+}, E_e) KECD region, as reported in Fig. 6. Process II leads to the L_1 dissociation limit (DL), processes III, IV, VII to the $L_{2/3}$ DL, and processes V and VI to the $L_{4/5/6}$ DL.

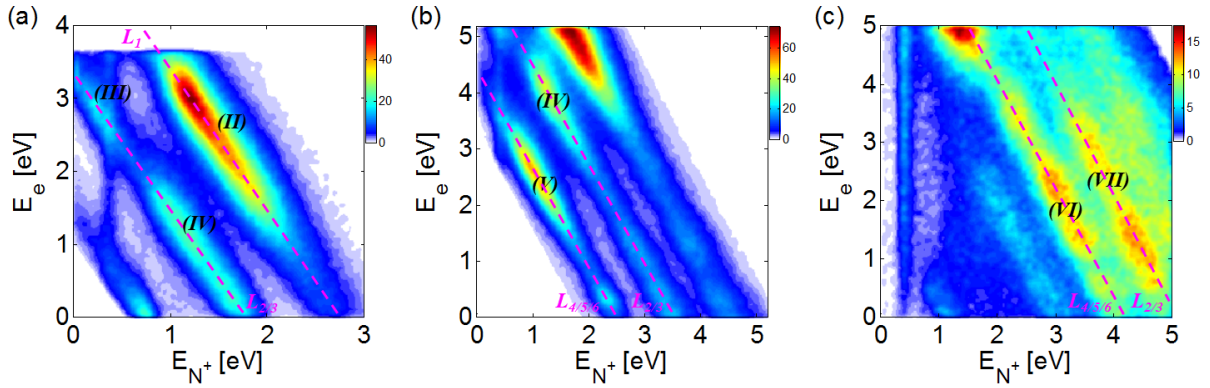

FIG. 6. (Color online) (E_{N+}, E_e) zoomed KECDs characterizing the DPI of NO induced by synchrotron radiation at (a) $h\nu = 26.35$ eV, (b) $h\nu = 29.45$ eV, (c) $h\nu = 32.55$ eV photon energies, selecting the E_e region where a 4π collection of electrons and N^+ fragments is ensured. Extraction fields of 40, 65 and 70 V/cm were employed, respectively. The pink dashed lines represent the dissociation limits (see Table II).

We first note that for the $h\nu = 23.25$ eV lowest studied energy, the DPI processes labeled II and III in Fig. 1(a), populated at threshold in the same 22.75-23.25 eV binding energy (BE) range and leading to the L_1 and $L_{2/3}$ DLs, respectively, display a similar structure involving four resolved vibrational states ($\Delta E_v \sim 80$ meV). Such a vibrational progression was assigned to the $NO^+(B\,^1\Pi(2))$ ionic state [39,40], a proposed assignment consistent with the characteristics of the measured circular dichroism in this energy range [12]. While process (III) remains localized at such 23-24 eV BEs at higher photon energy (*e.g.* $h\nu = 26.35$ eV in Fig. 6(a)), process (II) extends to higher BEs (23-24.7 eV) becoming the second most populated after process (I) with a BR ranging between 15 % ($h\nu = 26.35$ eV) and 30 % ($h\nu = 32.55$ eV).

MFPADs for processes (II) and (III) are displayed in Fig. 7(a) and (b) for $h\nu = 26.35$ eV for the selected orientations of the molecular axis: $\chi = 0°$ and $\chi = 90°$ relative to the polarization axis of linearly polarized light, and $\chi = 90°$ relative to the propagation axis of right-handed CPL. For process (III), they are very similar to those reported for the $NO^+(c\,^3\Pi)$ ionic state, with a major contribution of $p\sigma$, $d\sigma$ and $f\sigma$ partial waves for the $\chi = 0°$ orientation parallel to the polarization axis of linearly polarized light, and a $d\pi$ partial wave for the $\chi = 90°$ perpendicular orientation (see Section IV. B. and ref. [10]); the asymmetry parameter $\beta_{N+} \sim 0.90$ (± 0.05) also features a transition of strongly dominant parallel character. This further supports the assignment of process (III) to PI into the $NO^+(B\,^1\Pi(2))$ ionic state corresponding to ionization of the (4σ) molecular orbital (MO). Process (II) is characterized by drastically different MFPADs with a dominant $d\pi$ partial wave contribution for $\chi = 0°$, and a shape for $\chi = 90°$ which can be described as resulting from interferences between $s\sigma$, $d\sigma$ and $d\delta$ partial waves [11]. Therefore, although process (II) includes a contribution of PI into the $NO^+(B\,^1\Pi(2))$ ionic state at threshold, MFPADs at higher photon energies are the signature of a PI process dominated by ionization of a MO of π symmetry, assigned to

ionization into the $NO^+(B'\,^1\Sigma^+(3), (1\pi)^{-1})$ ionic state. They also correspond to a significantly lower β_{N+} asymmetry parameter, decreasing from 0.35 to -0.55 (± 0.05) when the photon energy increases up to 32.55 eV.

These characteristic features compare fairly well with the features in the computed MFPADs displayed in Fig. 7(d) and (e) for ionization into the $NO^+(B'\,^1\Sigma^+(3))$ and $NO^+(B\,^1\Pi(2))$ ionic states, respectively. We note that while these two processes behave according to the selection rules for $(1\pi)^{-1}$ and $(4\sigma)^{-1}$ one-electron ionization channels, the electronic configuration of the initial neutral states inferred from the MCSCI calculation involve an additional $(5\sigma)^1(1\pi)^3(2\pi)^2$ and $(5\sigma)^2(1\pi)^2(2\pi)^2$ two-electron component, respectively.

Processes IV and V display very comparable MFPADs (Fig. 7(c)) which resemble that of processes I and III, although the $d\pi$ character of the MFPAD for $\chi = 90°$ is not constrained to the ($\phi_e = 0°$ and $\phi_e = 180°$) plane as found earlier, and here rather displays a quasi-cylindrical symmetry about the molecular axis. These features are consistent with the calculation corresponding to ionization into the $NO^+(^3\Pi(4))$ state, which is dominated by the two-electron electronic configuration $(5\sigma)^1(1\pi)^3(2\pi)^2$, although the imprint of the perpendicular orientation into the MFPAD for circular polarization is more prominent in the measured MFPADs. The lower positive $\beta_{N+} \sim 0.4$-0.5 asymmetry parameter is also in fair agreement with the calculations. We stress that due to the repulsive character of the ionic states at such excitation energies, some of the selected processes involve a relatively extended E_e energy distribution, and might thereby involve the contribution from different ionic states along the dissociation in the KECDs.

The calculation providing the β_{N+} asymmetry parameters, which characterize the symmetry of the NO excited states in the continuum, confirms a clear distinction between ionization into the NO^+ states of Π ($\beta_{N+} > 0$) or Σ ($\beta_{N+} < 0$) symmetry in the studied XUV energy range (see Appendix). We also observe that the circular dichroism parameter is a sensitive probe of the ionization reaction, which involves both the symmetry of the ionized MO and the relative phases of the scattered partial waves as discussed earlier [12].

Finally, we note that for PI into the highly excited states corresponding to the processes labeled VI and VII in the zoomed KECD reported at $h\nu = 32.55$ eV, lying at 28.5-32.5 eV BEs, the measured MFPADs are comparable and display features also observed in the open $O^+ + N$ DLs. These do not abide by the classification of ionic states discussed above: they are characterized by sizeable positive $\beta_{N+} \sim 1$ asymmetry parameters, an overall shape of the $\chi = 0°$ MFPAD pointing to partial waves of $d\pi$ symmetry, and a vanishing CDAD. We attribute such features to the role of NO^+ Rydberg states converging to the $NO^{++}(X\,^2\Sigma)$ doubly charged ion addressed in previous studies in this binding energy region (*e.g.* ref. [40] and ref. therein). The present MCSCI calculations do not include such channels since there are no diffuse, Rydberg-like, orbitals included in the description of the bound ionic states.

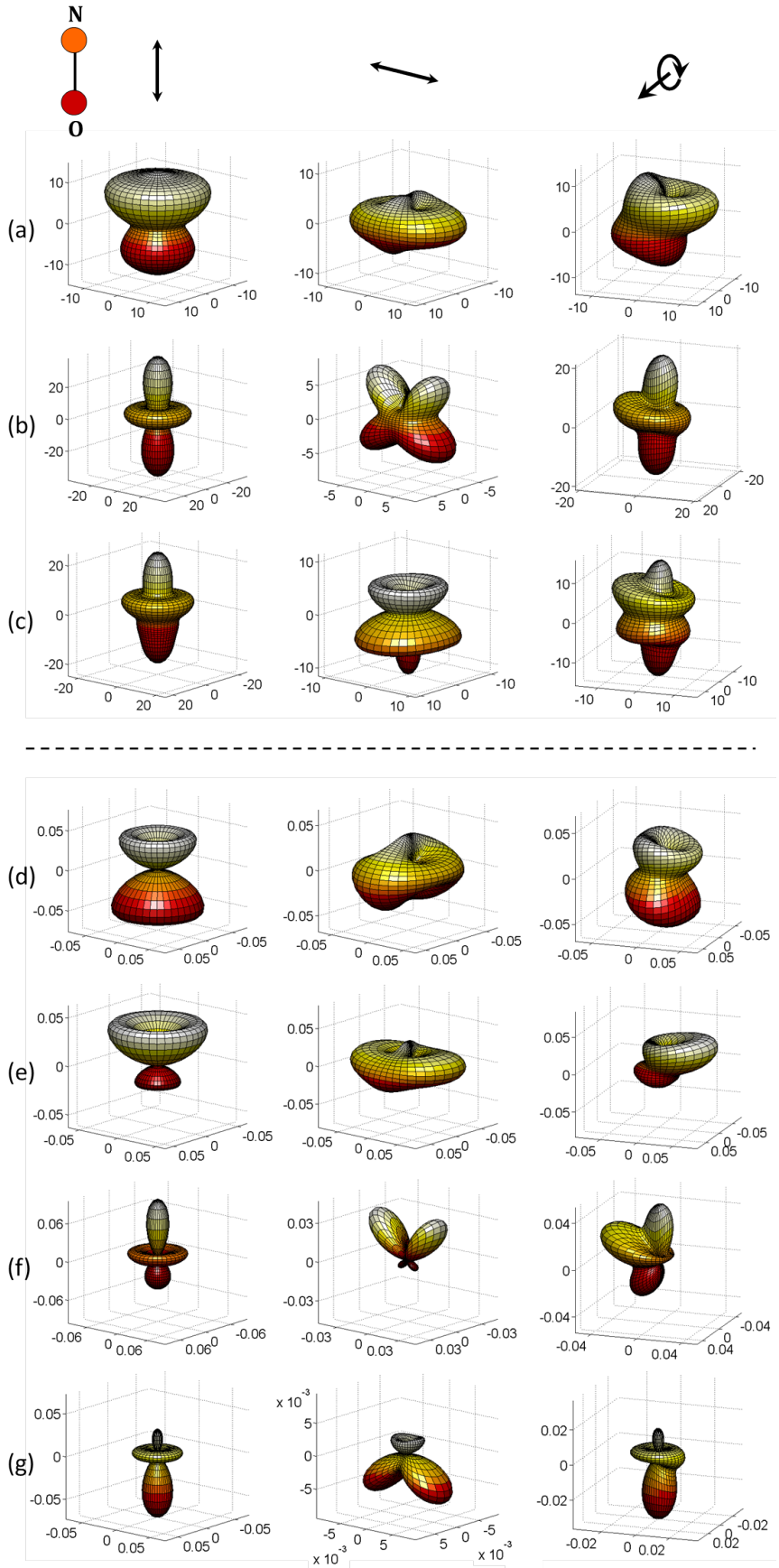

FIG. 7. (Color online) Measured (a-c) and computed in the velocity gauge (d-g) MFPADs. First and second columns: $I_{\chi=0^\circ}(\theta_e)$ and $I_{\chi=90^\circ}(\theta_e,\phi_e)$ relative to linearly polarized light, respectively; third column:

$I_{\chi=90°}(\theta_e,\phi_e)$ induced by right-handed CPL. (a) process (II) at $h\nu = 26.35$ eV, (b) process (III) at $h\nu = 26.35$ eV, (c) process (IV) at $h\nu = 29.45$ eV, (d-e) $B'\,^1\Sigma^+(3)$ state at $h\nu = 26.35$ eV and $h\nu = 29.45$ eV, (f) $B\,^1\Pi(2)$ state at $h\nu = 26.35$ eV, (g) $^3\Pi(4)$ state at $h\nu = 29.45$ eV. Experiment is arbitrarily normalized such that the total cross section $\int_0^\pi F_{00}(\theta_e)\sin(\theta_e)d\theta_e$ is equal to 1000.

VII. Conclusion

In this paper, we have reported results addressing the PI dynamics of the NO molecule in the extended 23-33 eV photon energy range across the σ^* shape resonance of the $NO^+(c\,^3\Pi)$ ionic state. The high resolving power of the KECDs ensures a good separation of the different induced DPI reactions, and allows for selecting one particular process of interest. As the studied photon energies correspond to the 15^{th}-21^{st} harmonics of a 800-nm fundamental wavelength laser, we also emphasized the complementarity of the present frequency-resolved synchrotron-based study with time-resolved studies in which PI is induced by broadband XUV attosecond pulses.

Using circularly polarized synchrotron radiation, we characterized the parallel and perpendicular transitions describing PI leading to the $NO^+(c\,^3\Pi)$ ionic state, as well as the associated circular dichroism in the molecular frame (CDAD). Measured MFPADs and dynamical parameters are in good agreement with the reported MCSCI calculations. For the purpose of molecular polarimetry, *e.g.* as an *in situ* tool for polarization analysis in high harmonic spectroscopy, the reported benchmark values for $F_{11}(\theta_e)$ and $CDAD(\theta_e)$ parameters constitute references for retrieving the amplitude and sign of the s_3 Stokes parameter.

Finally, we characterized the spectroscopy of new DPI processes into highly excited states of NO^+ induced in the considered 23-33 eV photon energy range and resolved in the presented KECDs. Assignments have been given based on the comparison of the experimental results with MCSCI calculations at the level of the β_{N+} asymmetry parameters and MFPADs.

Acknowledgments

We gratefully acknowledge L. Nahon, DESIRS beamline manager, and G. Garcia, beamline scientist, for fruitful cooperation, J. F. Gil for technical support on the beamline, and the SOLEIL general staff for smoothly operating the facility. We are grateful to E. Bouisset and S. Lupone from ISMO for their technical support. The work performed at Lawrence Berkeley National Laboratory was supported by the U.S. Department of Energy, Office of Science, Basic Energy Sciences, Chemical Sciences, Geosciences, and Biosciences Division under Contract DE-AC02-05CH11231.

Appendix: computed cross sections and asymmetry parameters

Here we present the computed total cross sections (Fig. 8) and asymmetry parameters (Fig. 9 and 10) for the states discussed in the paper for which the MFPADs are presented.

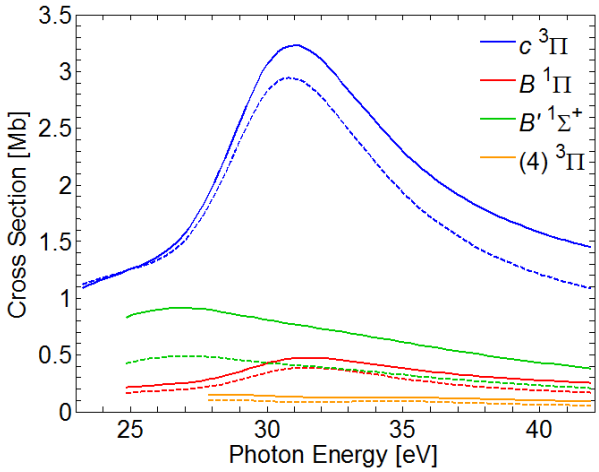

FIG. 8. (Color online) Total cross sections computed for ionization leading to the $c\,^3\Pi$ state (blue) from calculation "a", to the $B\,^1\Pi$ (red) and $B'\,^1\Sigma^+$ (green) states from calculation "b", and to the (4) $^3\Pi$ state (orange) from calculation "c". The different calculations are described in the Methods (Section II. C.). Solid lines are computed in the length form and the dashed lines in the velocity form.

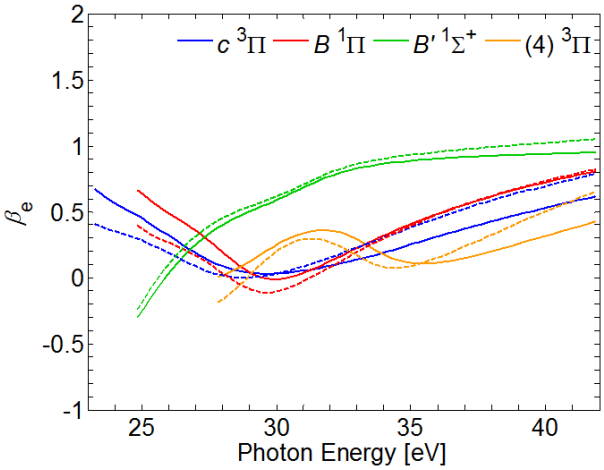

FIG. 9. (Color online) Photoelectron asymmetry parameters computed for ionization leading to the $c\,^3\Pi$ state (blue) from calculation "a", to the $B\,^1\Pi$ (red) and $B'\,^1\Sigma^+$ (green) states from calculation "b", and to the (4) $^3\Pi$ state (orange) from calculation "c". The different calculations are described in the Methods (Section II. C.). Solid lines are computed in the length form and the dashed lines in the velocity form.

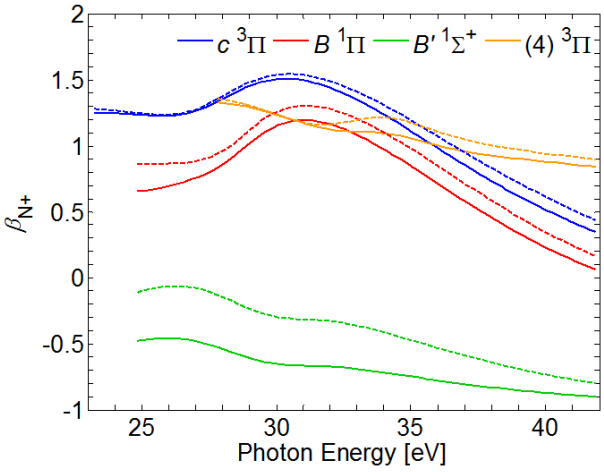

FIG. 10. (Color online) Ion asymmetry parameters computed for ionization leading to the $c\,^3\Pi$ state (blue) from calculation "a", to the $B\,^1\Pi$ (red) and $B'\,^1\Sigma^+$ (green) states from calculation "b", and to the (4) $^3\Pi$ state (orange)

from calculation “c”. The different calculations are described in the Methods (Section II. C.). Solid lines are computed in the length form and the dashed lines in the velocity form.

References

[1] K. L. Reid, Mol. Phys. **110**, 131 (2012).

[2] S. Motoki, J. Adachi, K. Ito, K. Ishii, K. Soejima, A. Yagishita, S. K. Semenov, and N. A. Cherepkov, Phys. Rev. Lett. **88**, 063003 (2002).

[3] O. Geßner, Y. Hikosaka, B. Zimmermann, A. Hempelmann, R. R. Lucchese, J. H. D. Eland, P.-M. Guyon, and U. Becker, Phys. Rev. Lett. **88**, 193002 (2002).

[4] M. Lebech, J. C. Houver, D. Dowek, and R. R. Lucchese, Phys. Rev. Lett. **96**, 073001 (2006).

[5] A. Landers, Th. Weber, I. Ali, A. Cassimi, M. Hattass, O. Jagutzki, A. Nauert, T. Osipov, A. Staudte, M. H. Prior, H. Schmidt-Böcking, C. L. Cocke, and R. Dörner, Phys. Rev. Lett. **87**, 013002 (2001).

[6] T. Jahnke, Th. Weber, A. L. Landers, A. Knapp, S. Schössler, J. Nickles, S. Kammer, O. Jagutzki, L. Schmidt, A. Czasch, T. Osipov, E. Arenholz, A. T. Young, R. Díez Muiño, D. Rolles, F. J. García de Abajo, C. S. Fadley, M. A. Van Hove, S. K. Semenov, N. A. Cherepkov, J. Rösch, M. H. Prior, H. Schmidt-Böcking, C. L. Cocke, and R. Dörner, Phys. Rev. Lett. **88**, 073002 (2002).

[7] T. Osipov, T. N. Rescigno, T. Weber, S. Miyabe, T. Jahnke, A. S. Alnaser, M. P. Hertlein, O. Jagutzki, L. P. H. Schmidt, M Schöffler, L. Foucar, S. Schössler, T. Havermeier, M. Odenweller, S. Voss, B. Feinberg, A. L. Landers, M. H. Prior, R Dörner, C. L. Cocke, and A. Belkacem, J. Phys. B At. Mol. Opt. Phys. **41**, 091001 (2008).

[8] X.-J. Liu, H. Fukuzawa, T. Teranishi, A. De Fanis, M. Takahashi, H. Yoshida, A. Cassimi, A. Czasch, L. Schmidt, R. Dörner, K. Wang, B. Zimmermann, V. McKoy, I. Koyano, N. Saito, and K. Ueda, Phys. Rev. Lett. **101**, 083001 (2008).

[9] A. Lafosse, M. Lebech, J. C. Brenot, P. M. Guyon, O. Jagutzki, L. Spielberger, M. Vervloet, J. C. Houver, and D. Dowek, Phys. Rev. Lett. **84**, 5987 (2000).

[10] M. Lebech, J. C. Houver, A. Lafosse, D. Dowek, C. Alcaraz, L. Nahon, and R. R. Lucchese, J. Chem. Phys. **118**, 9653 (2003).

[11] A. Lafosse, J. C. Brenot, P. M. Guyon, J. C. Houver, A. V. Golovin, M. Lebech, D. Dowek, P. Lin, and R. R. Lucchese, J. Chem. Phys. **117**, 8368 (2002).

[12] D. Dowek, M. Lebech, J. C. Houver, and R. R. Lucchese, Mol. Phys. **105**, 1757 (2007).

[13] D. Dowek, J. F. Pérez-Torres, Y. J. Picard, P. Billaud, C. Elkharrat, J. C. Houver, J. L. Sanz-Vicario, and F. Martín, Phys. Rev. Lett. **104**, 233003 (2010).

[14] D. Dowek and R. R. Lucchese, in *Dyn. Process. At. Mol. Phys.* (Bentham, Bussum, The Netherlands, 2012), pp. 57–95.

[15] M. Born and E. Wolf, *Principles of Optics* (Pergamon, New York, 1980).

[16] K. Veyrinas, C. Elkharrat, S. Marggi Poullain, N. Saquet, D. Dowek, R. R. Lucchese, G. A. Garcia, and L. Nahon, Phys. Rev. A **88**, 063411 (2013).

[17] W. B. Li, R. Montuoro, J. C. Houver, L. Journel, A. Haouas, M. Simon, R. R. Lucchese, and D. Dowek, Phys. Rev. A **75**, 052718 (2007).

[18] K. Veyrinas, PhD Thesis: Photoémission Dans Le Référentiel Moléculaire : Une Sonde de La Dynamique Électronique et Nucléaire et de l’état de Polarisation Du Rayonnement Ionisant, Université Paris-Sud 11, U.F.R. Scientifique d’Orsay, 2015.

[19] S. J. Weber, B. Manschwetus, M. Billon, M. Böttcher, M. Bougeard, P. Breger, M. Géléoc, V. Gruson, A. Huetz, N. Lin, Y. J. Picard, T. Ruchon, P. Salières, and B. Carré, Rev. Sci. Instrum. **86**, 033108 (2015).

[20] K. Veyrinas, V. Gruson, S. J. Weber, L. Barreau, T. Ruchon, J.-F. Hergott, J.-C. Houver, R. R. Lucchese, P. Salières, and D. Dowek, Faraday Discuss. **194**, 161 (2016).
[21] L. Barreau, K. Veyrinas, V. Gruson, S. J. Weber, T. Auguste, J.-F. Hergott, F. Lepetit, B. Carré, J.-C. Houver, D. Dowek, and P. Salières, Nat. Commun. **9**, 4727 (2018).
[22] L. Nahon, N. de Oliveira, G. A. Garcia, J.-F. Gil, B. Pilette, O. Marcouillé, B. Lagarde, and F. Polack, J. Synchrotron Radiat. **19**, 508 (2012).
[23] L. Nahon and C. Alcaraz, Appl. Opt. **43**, 1024 (2004).
[24] A. Lafosse, J. C. Brenot, A. V. Golovin, P. M. Guyon, K. Hoejrup, J. C. Houver, M. Lebech, and D. Dowek, J. Chem. Phys. **114**, 6605 (2001).
[25] M. Lebech, J. C. Houver, and D. Dowek, Rev. Sci. Instrum. **73**, 1866 (2002).
[26] R. R. Lucchese, A. Lafosse, J. C. Brenot, P. M. Guyon, J. C. Houver, M. Lebech, G. Raseev, and D. Dowek, Phys. Rev. A **65**, 020702 (2002).
[27] R. E. Stratmann and R. R. Lucchese, J. Chem. Phys. **102**, 8493 (1995).
[28] R. E. Stratmann, R. W. Zurales, and R. R. Lucchese, J. Chem. Phys. **104**, 8989 (1996).
[29] T. H. Dunning, J. Chem. Phys. **90**, 1007 (1989).
[30] R. A. Kendall, T. H. Dunning, and R. J. Harrison, J. Chem. Phys. **96**, 6796 (1992).
[31] H.-J. Werner, P. J. Knowles, G. Knizia, F. R. Manby, and M. Schütz, Wiley Interdiscip. Rev. Comput. Mol. Sci. **2**, 242 (2012).
[32] K. P. Huber and G. Herzberg, *Molecular Spectra and Molecular Structure IV. Constants of Diatomic Molecules* (Van Nostrand Reinhold Co., New York, 1979).
[33] D. L. Albritton, A. L. Schmeltekopf, and R. N. Zare, J. Chem. Phys. **71**, 3271 (1979).
[34] Y. Iida, F. Carnovale, S. Daviel, and C. E. Brion, Chem. Phys. **105**, 211 (1986).
[35] J. H. D. Eland and E. J. Duerr, Chem. Phys. **229**, 1 (1998).
[36] J. W. Gallagher, C. E. Brion, J. A. R. Samson, and P. W. Langhoff, J. Phys. Chem. Ref. Data **17**, 9 (1988).
[37] S. K. Semenov and N. A. Cherepkov, J. Phys. B At. Mol. Opt. Phys. **42**, 085101 (2009).
[38] J. H. D. Eland, M. Takahashi, and Y. Hikosaka, Faraday Discuss. **115**, 119 (2000).
[39] H. Partridge, S. R. Langhoff, and C. W. Bauschlicher, J. Chem. Phys. **93**, 7179 (1990).
[40] Y. Hikosaka, T. Aoto, K. Ito, Y. Terasaka, R. Hirayama, and E. Miyoshi, J. Chem. Phys. **128**, 044320 (2008).